

Mapping of cerebro-vascular blood perfusion in mice with skin and skull intact by Optical Micro-AngioGraphy at 1.3 μ m wavelength

Ruikang K Wang* and Sawan Hurst

Department of Biomedical Engineering, Oregon Health & Science University, Portland, OR 97237, USA

*Corresponding author: r.k.wang@bme.ogi.edu

<http://www.bme.ogi.edu/biomedicaloptics>

Abstract: Optical micro-angiography (OMAG) was developed to achieve volumetric imaging of the microstructures and dynamic cerebrovascular blood perfusion in mice with capillary level resolution and high signal-to-background ratio. In this paper, we present a high-speed and high-sensitivity OMAG imaging system by using an InGaAs line scan camera and broadband light source at 1.3 μ m wavelength for enhanced imaging depth in tissue. We show that high quality imaging of cerebrovascular blood perfusion down to capillary level resolution with the intact skin and cranium are obtained *in vivo* with OMAG, without the interference from the blood perfusion in the overlaying skin. The results demonstrate the potential of 1.3 μ m OMAG for high-speed and high-sensitivity imaging of blood perfusion in human and small animal studies.

©2007 Optical Society of America

OCIS codes: 170.4500 (optical coherence tomography); 170.3880 (medical and biological imaging); 999.9999 (Optical micro-angiography); 999.9999 (Cerebro-vascular blood perfusion).

References and links

1. D. M. McDonald and P. L. Choyke, "Imaging of angiogenesis: from microscope to clinic," *Nat. Med.* **9**, 713-725 (2003).
2. D. Malonek, U Dirnagl, U Lindauer, K Yamada, I Kanno, and A Grinvald, "Vascular imprints of neuronal activity: relationships between the dynamics of cortical blood flow, oxygenation, and volume changes following sensory stimulation," *Proc. Natl. Acad. Sci. USA* **94**, 14826-14831 (1997).
3. K. Hossmann, "Viability thresholds and the penumbra of focal ischemia," *Ann Neurol* **36**, 557-565 (1994).
4. T. P. Padera, B. R. Stoll, P. T. So, and R. K. Jain, "Conventional and high speed intravital multiphoton laser scanning microscopy of microvasculature, lymphatics, and leukocyte-endothelial interactions," *Mol. Imaging* **1**, 9-15 (2002).
5. R. K. Jain, "Delivery of molecular medicine to solid tumors: lessons from *in vivo* imaging of gene expression and function," *J. Controlled Release* **74**, 7-25 (2001).
6. O. Sakurada, C. Kennedy, J. Jehle, J. D. Brown, G. L. Carbin, and L. Sokoloff, "Measurement of local cerebral blood flow with iodo [14C] antipyrine," *Am J. Physiol.* **234**, H59-66 (1978).
7. F. Calamante, D. L. Thomas, G. S. Pell, J. Wiersma, and R. Turner, "Measuring cerebral blood flow using magnetic resonance imaging techniques," *J Cereb Blood Flow Metab* **19**, 701-735 (1999).
8. W. D. Heiss, R. Graf, K. Wienhard, J. Lottgen, R. Saito, T. Fujita, G. Rosner, and R. Wagner, "Dynamic penumbra demonstrated by sequential multitracer PET after middle cerebral artery occlusion in cats," *J Cereb Blood Flow Metab* **14**, 892-902 (1994).
9. A. Grinvald, E. Lieke, R. D. Frostig, C. D. Gilbert, and T. N. Wiesel, "Functional architecture of cortex revealed by optical imaging of intrinsic signals," *Nature* **324**, 361-364 (1986).
10. A. K. Dunn, H. Bolay, M. A. Moskowitz, and D. A. Boas, "Dynamic imaging of cerebral blood flow using Laser Speckle," *J. Cereb. Blood Flow Metab.* **21**, 195-201 (2001).
11. A. N. Nielsen, M. Fabricius, and M. Lauritzen. "Scanning laser-Doppler flowmetry of rat cerebral circulation during cortical spreading depression," *J. Vasc. Res.* **37**, 513-522 (2000).
12. X. D. Wang, Y. Pang, G. Ku, X. Xie, G. Stoica, and L.-H. Wang, "Non-invasive laser-induced photoacoustic tomography for structural and functional imaging of the brain *in vivo*," *Nat. Biotechnol.* **21**, 803-806 (2003).
13. H. F. Zhang, K. Maslov, G. Stoica, and L. H. V. Wang, "Functional photoacoustic microscopy for high-resolution and noninvasive *in vivo* imaging," *Nat. Biotechnol.* **24**, 848-851 (2006).

14. T. Misgeld and M. Kerschensteiner, "In vivo imaging of the diseased nervous system." *Nat. Rev. Neurosci.* **7**, 449-463 (2006).
15. R. K. Wang, S. L. Jacques, Z. Ma, S. Hurst, S. Hanson, and A. Gruber, "Three dimensional optical angiography," *Opt. Express* **15**, 4083-4097 (2007).
16. G. Hausler and M. W. Lindner, "Coherence radar and Spectral radar- new tools for dermatological diagnosis," *J. Biomed. Opt.* **3**, 21-31 (1998).
17. Z. P. Chen, T. E. Milner, S. Srinivas, *et al.*, "Noninvasive imaging of in vivo blood flow velocity using optical Doppler tomography," *Opt. Lett.* **22**, 1119-1121 (1997).
18. B. R. White, M. C. Pierce, N. Nassif, *et al.*, "In vivo dynamic human retinal blood flow imaging using ultra-high-speed spectral domain optical Doppler tomography," *Opt. Express* **11**, 3490-3497 (2003).
19. R. K. Wang and Z. H. Ma, "Real-time flow imaging by removing texture pattern artifacts in spectral-domain optical Doppler tomography," *Opt. Lett.* **31**, 3001-3003 (2006).
20. R. K. Wang, Z. Ma, and S. J. Kirkpatrick, "Tissue Doppler optical coherence elastography for real time strain rate and strain mapping of soft tissue," *Appl. Phys. Lett.* **89**, 144103 (2006).
21. Y. Pan, and D. L. Farkas, "Non-invasive imaging of living human skin with dual-wavelength optical coherence tomography in two and three dimensions," *J. Biomed. Opt.* **3**, 446-465 (1998).
22. B. E. Bouma and G. J. Tearney, "Clinical imaging with optical coherence tomography," *Acad. Radiol.* **9**, 942-953 (2002).
23. L. Carrion, M. Lestrade, Z. Xu, G. Touma, R. Maciejko, and M. Bertrand, "Comparative study of optical sources in the near infrared for optical coherence tomography applications," *J. Biomed. Opt.* **12**, 014017 (2007).
24. S. H. Yun, G. J. Tearney, B. E. Bouma, B. H. Park, and J. F. de Boer, "High-speed spectral-domain optical coherence tomography at 1.3 μm wavelength," *Opt. Express* **11**, 3598-3604 (2003).
25. B. H. Park, M. C. Pierce, B. Cense, S. H. Yun, M. Mujat, G. J. Tearney, B. E. Bouma, and J. F. de Boer, "Real-time fiber-based multi-functional spectral-domain optical coherence tomography at 1.3 μm ," *Opt. Express* **13**, 3931-3944 (2005).
26. R. K. Wang, "In vivo full range complex Fourier Domain optical coherence tomography," *Appl. Phys. Lett.* **90**, 054103 (2007).
27. R. K. Wang and Z. H. Ma, "A practical approach to eliminate autocorrelation artefacts for volume-rate spectral domain optical coherence tomography," *Phys. Med. Biol.* **51**, 3231-3239 (2006).
28. C. Dorrer, N. Belabas, J. P. Likforman, and M. Joffre, "Spectral resolution and sampling issues in Fourier-transform spectral Interferometry," *J. Opt. Soc. Am. B* **17**, 1795-1802 (2000).
29. R. K. Wang, "Modelling optical properties of soft tissue by Fractal Distribution of Scatters," *J. Mod. Opt.* **47**, 103-120 (2000).

1. Introduction

The ability to accurately visualize micro-vascular networks under normal and diseased conditions is critical for evaluating the emerging therapeutic strategies, such as in the development of potential drugs to support or limit neovascular growth [1]. Another example is in the treatment and diagnosis of neural vascular diseases where the cerebral blood perfusion is related to the normal and pathophysiologic conditions of brain metabolism [2, 3]. Technical constraints currently limit most microvascular imaging to two dimensions, however three-dimensional (3D) visualization of vascular image data is often required in order to reveal the detailed architecture of the microvascular network so that the volumetric rheology and perfusion status of the tissue can be quantified [4,5].

Numerous techniques have been applied to image the cerebral blood flow (CBF) and volume changes. Conventional X-ray carotid angiography is an excellent clinical tool; however, it is invasive and not suitable for small animal studies. Although autoradiographic methods provide endpoint 3D spatial information, they contain no information about the dynamic CBF evolution [6]. Methods based on magnetic resonance imaging [7] and positron emission tomography [8] provide spatial maps of CBF but are limited in their temporal and spatial resolution. Optical intrinsic signal imaging [9], laser speckle imaging [10] and laser-Doppler flowmetry techniques [11] have the desired high spatial resolution, but are limited to two-dimensional mapping of CBF and require surgical opening or substantial thinning of the cranium during the study. Photoacoustic imaging, based on thermal-acoustic phenomena resulting from the strong light absorption of blood and the subsequent thermo-elastic expansion, has recently been reported to map vascular structures deep within the brain of small animals [12,13]. However, the spatial ($\sim 100 \mu\text{m}$) resolution of this approach is limited

by the viscoelastic filtering of higher acoustic frequencies by the tissue. Moreover, blood flow information is not forthcoming with this method. Confocal microscopy, a widely used technique that is capable of ultrahigh resolution mapping of the cerebrovasculature [14], also requires the removal of intervening bone due to its limited imaging depth (up to 300 μm) and the use of injected fluorescent tissue markers.

Optical micro-angiography (OMAG) [15] is a recently developed imaging method, capable of resolving 3D distribution of dynamic blood perfusion at the capillary level within microcirculatory beds *in vivo*. The imaging contrast of blood perfusion is based on the endogenous light scattering from the moving blood cells within biological tissue; thus no exogenous contrasting agents are necessary. This is achieved by efficient separation of the moving scattering elements from the static scattering ones within tissue through the OMAG hardware associated with mathematical analysis of the optical scattering signals from an illuminated sample. Its development has its origin in the Fourier domain optical coherence tomography (FDOCT) [16]. OMAG improves over previous methods, e.g. FDOCT and Doppler OCT [17-20] by introducing a constant frequency modulation f_M into the time-varying spectral interferograms at the time when the probing beam is scanned over the sample. The introduction of f_M in the interferograms was achieved by linear translation of the reference mirror in the interferometer, synchronized with the OCT cross-sectional (B scan) imaging. This makes it possible to separate the light scattering signals backscattered from the moving particles, such as moving blood cells, from those backscattered from the static particles, such as bulk tissue, leading to high resolution mapping of dynamic blood perfusion down to capillary levels within thick tissue sample *in vivo*. In essence, the OMAG method maps the scattering signals from the moving particles into one image, i.e. flow image, and from the static particles into a second image, i.e. microstructural image. The previous reported OMAG system used light source centered at $\sim 840\text{nm}$ that has shown capable of imaging cerebro-vascular blood perfusion in mice with the cranium intact [15]. It would be desirable that the cerebro-vascular blood perfusion can be accessed without removal of the overlying skin so that the possible complications of dynamic blood flow due to surgical interventions can be minimized.

Because it is a variation of FDOCT method, OMAG has almost the same advantages and disadvantages as those possessed by FDOCT. In the development of FDOCT, one of the efforts is to improve the several system characteristics for *in vivo* imaging applications, these including imaging resolution, signal-to-noise ratio, and imaging depth. These parameters are strongly dependent on the light source characteristics, especially on its emission wavelength. As the optical properties of biological tissue, for example absorption and scattering, have strong relation with the optical frequency (wavelength), OCT/OMAG imaging depth and contrast are no doubt dependent on the emission wavelength of the illuminating light source used. Previous investigations in the development of OCT have shown that, for a highly scattering biological tissue, enhanced imaging depth for light source centered at $\sim 1300\text{nm}$ wavelength can be resulted when compared to that centered at $\sim 820\text{nm}$ [21-23]. This conclusion therefore also holds for OMAG imaging modality.

In this paper, we demonstrate a high-speed, high sensitivity OMAG imaging system operating at a central wavelength of $1.3\mu\text{m}$ for maximum imaging depth in tissue. By using an InGaAs line scan camera as the detecting component in the spectrometer, we have obtained high quality *in vivo* OMAG images of cerebro-vascular blood perfusion in mice with the skin and skull intact. To the best of our knowledge, since the development of OCT, this is the first time that trans-dermal and trans-cranial cerebral blood perfusion can be imaged in 3D at the capillary level resolution.

2. OMAG system setup

A schematic of the OMAG system operating at $1.3\mu\text{m}$ is shown in Fig. 1. Because OMAG has its origin in Fourier domain OCT, the system layout is similar to that of $1.3\mu\text{m}$ spectral domain OCT [24, 25] and our previous OMAG system operating at 840nm [15]. The light

source is a broadband, superluminescent diode (SLD) with full-width-half-maximum (FWHM) of 48nm centered at 1.3 μ m (Denselight, Singapore). The total output power was 10mW. This light source yielded a measured axial resolution of 15 μ m in air. The light was coupled into the spectral domain fiber-based Michelson interferometer via a broadband optical circulator (Newport, USA). The sample light was delivered to a sample-arm imaging probe that was focused into the sample by an objective lens ($f=50$ mm) with a focal spot of $\sim 20\mu$ m. In order to perform 3D imaging of tissue sample *in vivo*, an X-Y galvanometer scanner (GSI Lumonics, USA) with a scanning priority in X direction was used to scan the focused beam spot over the sample. The X-scanner was driven by 10Hz saw tooth waveform to provide transverse scanning over 2.5mm (B scan) at the sample, while the Y-scanner was driven by 0.02Hz saw tooth waveform that provided the beam scanning in the elevational direction of also 2.5mm. The reference arm of the interferometer had an adjustable delay reference-mirror and dispersion was matched between the sample and reference arms by use of optical materials with different thickness. The reference mirror was mounted onto a piezo-translation stage (Physik Instrument, Germany) that was also driven by a saw tooth waveform with an amplitude equivalent to the maximum reference delay of 40 μ m. This saw tooth waveform was synchronized with that used to drive the X-scanner and provided a constant modulation frequency of $f_M = \sim 0.62$ kHz in the spatial spectral interferograms when the probe beam was scanned over the sample. Thus, the minimum blood flow velocity that can be measured by this system is 0.4 mm/s as determined by the constant velocity of the moving mirror driven by the piezo-translation stage [15]. In addition, polarization controllers were used in the reference, sampling and detection arms in order to maximize the spectral interference fringe contrast at the detector. Also, a 633 nm visible light from a laser diode was coupled into the interferometer for ease of the positioning during imaging.

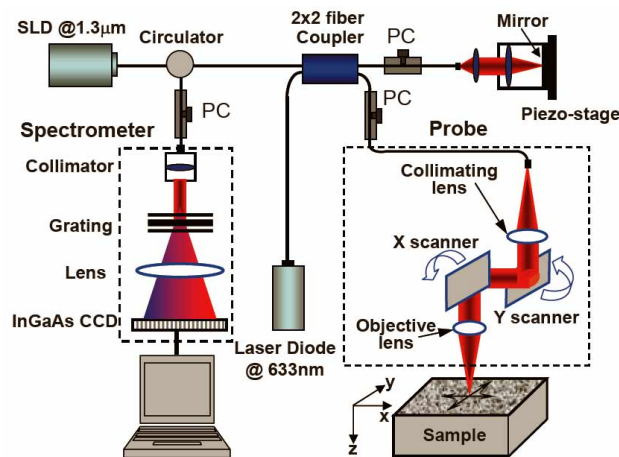


Fig. 1. Schematic of the OMAG system operating at 1.3 μ m where SLD represents the superluminescent diode and PC the polarization controller.

The output of the interferometer was routed into a spectrometer via the optical circulator. The spectrometer consists of an IR achromatic doublet $f = 50$ mm fiber collimating lens, a 1200 line/mm volume phase holographic grating (Wasatch Photonics, USA) with 80% efficiency, and an $f = 190$ mm lens that images the spectral interference onto a 512 element infrared InGaAs linescan camera (Sensors Ltd. USA). The optical efficiency of the spectrometer defined as the power incident on the camera detector array divided by the power in the fiber is approximately 78%. The camera has a 14-bit resolution with a maximum line scan rate of 20.5 kHz. The camera integration time was set at 60 μ s for imaging, allowing 40 μ s to download the spectral data from camera (512 pixels, A scan) to the host computer (Pentium IV, 3.2 GHz, 2 GB RAM) via CameraLink™ and a high-speed frame grabber board (PCI 1428, National Instruments, USA). This means that the camera line scan rate was 10

kHz for the current study. According to the sampling theorem, the maximum speed of blood flow in the direction of incident beam that can be detected by this system setup is 3.25mm/s, equivalent to the Doppler frequency of ± 5 kHz. The spectrometer was calibrated over the measured bandwidth by comparing the spectrum registered by the InGaAs camera with a commercial optical spectrum analyzer (Anritsu MS971013B, Japan). The spectrometer had a designed spectral resolution of 0.159 nm. Because OMAG is an *in vivo* full range complex imaging technique [26], this spectral resolution results in an optical ranging of approximately 5.8 mm in air, i.e. the full depth in the Fourier space, (z axis shown in the Fig. 1), where the positive frequency space (2.9 mm) was used for micro-structural imaging and the negative frequency space (2.9 mm) for flow imaging. The signal sensitivity of 105 dB was measured at $z=+0.3$ mm and dropped to 95 dB at $z=+2.5$ mm when the camera integration time was set at 60 μ s. During the imaging, the actions for probe scanning, piezo-stage translation, data acquisition, data storage and hand-shaking between them were controlled by a custom software package written in Labview[®] language.

Volumetric imaging data was collected by scanning the probe beam spot using the X-Y scanner. In the x direction, there were 1000 discrete points measured over 2.5 mm that makes up a data matrix of 1000 by 512 elements (slice, B scan). In the y direction, there were 500 discrete points over 2.5mm. Thus, a final volume data cube (spectrograms) of 1000 by 500 by 512 (x - y - z) voxels was built from which the 3-dimensional OMAG structural and flow images were computed. It took 50 seconds to obtain such volume data cube using the current setup.

In order to enhance the final OMAG image quality, data-preprocessing was necessary on the raw volumetric spectrogram data set. First, all the spectral interferograms in each slice along the x -direction were ensemble-averaged at each wavelength to obtain a reference spectrum, which was then subtracted from each A scans. This operation effectively removes/minimizes autocorrelation, self-cross correlation, and camera noise artifacts presented in the final OMAG images [27] that considerably improves the image quality. The subtracted spectral interferograms are then converted into the equal frequency space by use of the spline interpolation method as usually done in the FDOCT [28]. Note that before the operation of wavelength to frequency conversion, the spectral data of 512 pixels in each A scan was re-sampled into 1024 pixels by padding with zeros using the Fourier transformation method [28] so that the OCT signal fidelity is improved. Finally, the OMAG algorithm was applied to the pre-processed data set to compute the structural and flow images, i.e. Hilbert (x direction) and Fourier (frequency direction) transformations were performed in tandem [15]. Final OMAG structural and flow images were of the dimension of 1000 by 500 by 512 voxels (C scan), respectively. After scaling with an average refractive index of 1.4 for typical biological tissues [29], the C scan represented a physical volume dimension of $2.5 \times 2.5 \times 2.0$ mm³ (x - y - z).

3. Results

3.1 Performance assessment

To assess the imaging performances afforded by OMAG, we conducted a series of experiments. First, we used a homogeneous scattering phantom, an opaque granular plastic, to evaluate the background noise level. It is important because this metric directly relates to our ability to extract the useful signals from the noisy background. In order to test how the different A scan sampling density affects the OMAG results, we imaged the phantom with A-scan spatial sampling over B-scan (2.5mm) being 1000 and 2000 points, corresponding to 2.5 μ m and 1.25 μ m separation distance between adjacent A-scans, respectively. The results are shown in Fig. 2 where (A) is the conventional OCT/OMAG image available from the OMAG structural space, while (B) gives the result from the OMAG flow space. There is no visible improvement in the noise floor of the flow image when the A scan sampling density is dramatically increased (from 1000 to 2000 A scans over 2.5mm B scan in this case). To more clearly visualize this, Fig. 2(C) plots the noise floor level in the OMAG flow space, calculated as the ensemble average of the OMAG flow signal, from the images of Fig. 2(B) as functions

of depth in the phantom. Because the system sensitivity falls off over the depth due to the finite size of the detector in the camera, and also OCT/OMAG structural signal magnitude decays approximately exponentially along depth, the dependence of noise level on signal magnitude are also given in the plot, which is shown as the upper horizontal axis in Fig. 2(C). Also plotted are the noise floor levels from the two additional cases, i.e. 1) when the sampling arm was blocked, and 2) both the reference and sample arms were blocked, respectively. It is clear that the noise levels are close to the system noise floor when the sample arm was blocked for two different A sampling densities examined, indicating that the noise in OMAG is dominated by the light intensity fluctuation noise and system noise. On the other hand, it implies that the system was not operated at the shot-noise limited detection mode when compared with the system noise floor (see the bottom curve in Fig. 2(C)). Therefore, this noise level can still be further reduced if the light energy in the reference arm is optimized for imaging so that the shot-noise limited detection is achieved. In this particular experiment, we set the modulation frequency of $f_M = 0.3$ kHz in the spatial interferogram, equivalent to a velocity threshold of ~ 200 $\mu\text{m/s}$ for OMAG imaging. This performance gives superb ability for OMAG to detect the flow within the sample because the flow signal is with much high dynamic range, equivalent to the OCT system dynamic range which in this case is $>95\text{dB}$ within the imaging depth of 2.5mm. Note that this flow signal dynamic range is different from the flow velocity dynamic range. The latter is determined by the modulation frequency and the maximum scan rate of CCD used for imaging that is $[0.2 \ 3.25]$ mm/s for this study. More important, the signals at deeper imaging depth are without artifact noise which is important if we are imaging the microcirculation blood flow through the overlaying tissues, for example accessing the cortical blood perfusion through the skin and skull bone for mice imaging.

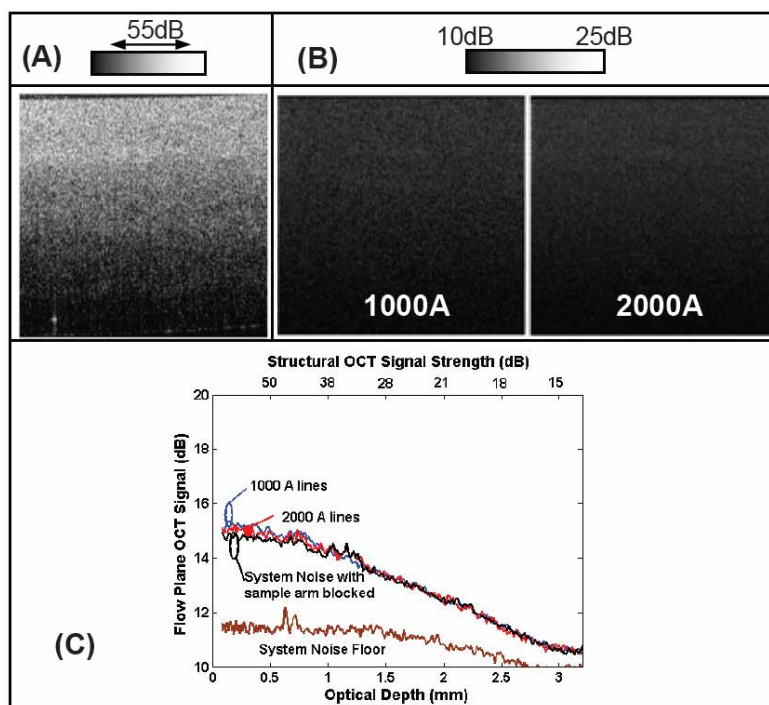


Fig. 2. Imaging of a solid scattering material to assess the noise level of OMAG imaging performance. 1000 and 2000 A scan spatial sampling density over 2.5 mm of B scan are given, respectively. (A) OCT/OMAG structural image, (B) OMAG flow image where there is almost no improvement when denser sampling approach is used, and (C) background noise level plotted as a function of depth in OMAG flow image, which results suggesting OMAG delivers superb flow imaging performance.

To evaluate the flow signals at the deeper imaging locations within sample, we used OMAG system to image the blood circulation within the finger nail bed of an adult volunteer. The *in vivo* OMAG imaging results are given in Fig. 3. The micro-circulations are located at the living nail bed which in this case is about $\sim 0.8\text{mm}$ beneath the nail surface. Despite attenuation of the OCT signals as well as optical heterogeneity of the nail plate and bed, OMAG clearly identifies the blood perfusion within the capillaries with good signal to background noise ratio. This attributes to that OMAG imaging is free of artifact noises along the imaging depth.

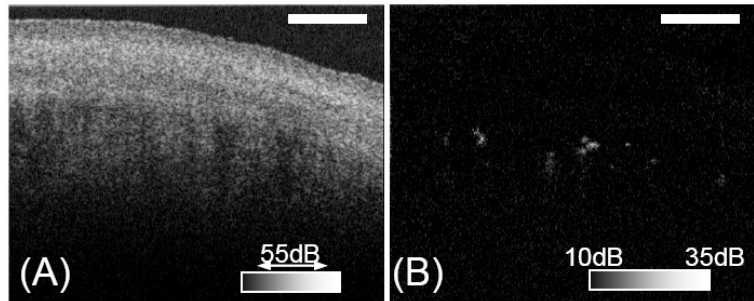


Fig. 3. *In vivo* imaging of the finger nail bed of an adult volunteer (41 years age). Shown is a B scan consisting of 1000 A scans across 2.5mm. (A) Structural OCT/OMAG image where the nail plate and bed can be clearly visualized. (B) OMAG flow image where it is evident that the capillary blood flows within nail bed are abundant. The white bar indicates $500\mu\text{m}$.

3.2. *In vivo* mouse imaging results

Next, we used the OMAG system to image the cerebro-vascular blood perfusion in mice with the intact skin and skull *in vivo*. All experiments were performed on C57Bl/6 male mice (Charles River Colony) which weighed 15 to 20 g and were approximately 3 months old. All the procedures were done using sterile technique and the mice were prepared for OMAG imaging 24 hours in advance by shaving their heads followed by an application of depilatory cream (Nair) to remove all remaining hair on the skin. For OMAG scans the animal was mounted on a custom made stereotaxic stage which stabilized the head. During imaging, the mouse was lightly anesthetized using 2% isoflurane (0.2L/min O₂, 0.8L/min air). The body temperature was maintained by a warming blanket and was kept between 36.7-37.1 C monitored by a rectal thermal probe. A drop of mineral oil was applied and spreaded uniformly on the skin of head before the imaging was taken place in order to minimize the strong skin surface reflection. After OMAG imaging, the animal was euthanized by cervical dislocation and digital images were taken (Roper Scientific Photometrics Coolsnap cf) of the head. Next the skin and skull on the head were carefully removed to expose the dorsal blood vessels of the brain which were then photographed to be compared with that from the OMAG imaging system. All animals were disposed of according to IACUC regulations. The protocol was approved by the Oregon Health & Sciences University Institutional Animal Care and Use Committee and was in compliance with the guidelines of the National Institutes of Health for care and handling of laboratory animals.

3-D OMAG images including structural morphology and blood perfusion were computed by evaluating the spectrogram data slice by slice, then re-combining to yield the 3-D volume dataset (x-y-z), from which high quality information regarding vasculature, blood flow and microstructures can be extracted. In the positive space of OMAG imaging method, there was obtained the 3-D localized microstructural image. Fig. 4 illustrates the 3D volume rendered image representing the structural information of the scanned tissue volume of $2.5 \times 2.5 \times 2.0$ (x-y-z) mm³, from which the histologically important layers such as skin, skull bone and grey matter are clearly identified. The average thicknesses of the skin and skull were estimated at $\sim 355\mu\text{m}$ and $\sim 188\mu\text{m}$, respectively. This 3-D image can be rotated and cut in any directions and planes so that the detailed morphological information within scanned volume can be

examined. It is clear that the 1.3 μm light source penetrated through the skin and skull bone, giving an opportunity to access to the cortex of the mouse brain for evaluating the brain activity without the need to remove the intervening skin and bone for imaging such as in confocal microscopy. However, it is difficult to visualize the blood flows within the scanned tissue from the structural image. Because red blood cells flow through all blood vessels including capillaries, acting as the moving scattering particles when exposed under the OMAG system, the blood flows can be precisely localized in the negative space in OMAG. As the positive and negative spaces are exactly mirrored, they can be folded to fuse a single volume image to localize with high precision the blood vessels within the tissue sample. Fig. 5(A) shows such a volume image that was resulted from by fusing the OMAG structural and flow images together, where a cut away view in the central area of micro-structural volume is used to more clearly appreciate how the blood vessels are oriented in the 3D volume.

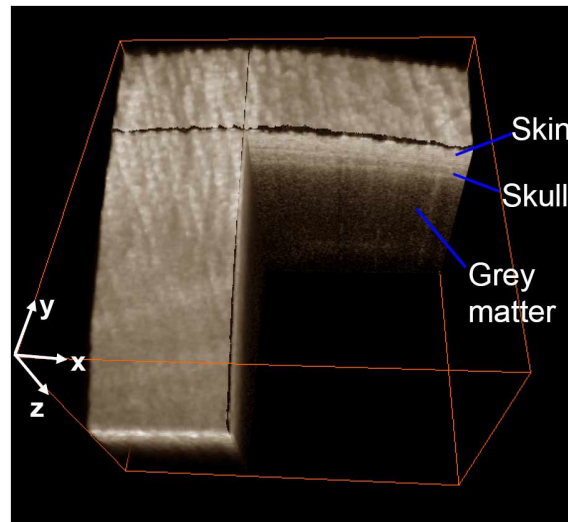


Fig. 4. Cut away view of volume image rendered from 3-D micro-structural images of the mouse head obtained by OMAG system *in vivo*, where the important tissue layers, such as skin, skull bone and grey matter are clearly identified. The volume image given has a physical dimension of $2.5 \times 2.5 \times 2.0 \text{ mm}^3$ in x-y-z direction as shown. See also the movie ([2.5Mbytes](#));

Because OMAG gives the depth-resolved blood perfusion image of the scanned tissue volume, the blood flows within the skin and brain cortex can be separated so that the quantification of cerebral vascular perfusion is possible without the interference from the blood perfusion located within the skin. The results are given in the right side of Fig. 5, where the x-y projections of blood flows existed within the skin that was detected by OMAG is shown in Fig. 5(B), while the cerebral blood perfusion is illustrated in Fig. 5(C). In obtaining the depth-resolved blood flow projection images, an image segmentation algorithm was used to separate the blood flow signals within skin from those within the brain cortex. The steps of segmentation algorithm included: 1) By utilizing the 3D OMAG structural image, such as Fig. 4, the skin surface was found by a simple intensity-threshold method. 2) The resulted skin surface found in step 1 was then smoothed in 3D space in order to improve the accuracy of the 3-D volume segmentation. 3) Two 3D masks were then generated, i.e. skin mask and brain mask. Skin mask covers the tissue volume $500 \mu\text{m}$ below the smoothed surface from step 2. This made sure that the bottom boundary of 3D skin mask was situated approximately within the skull bone. A further $1000 \mu\text{m}$ below the skin mask was then made up of the brain mask. 4) Because the OMAG structural image coins with the blood perfusion image, the two masks obtained in step 3 was applied to the OMAG blood perfusion image to generate two separate 3D flow images, one representing the signals from the skin and another from the mouse brain. 5) Finally, maximum amplitude projection (MAP) approach was used to project the

segmented blood flow images onto the x-y plane. This algorithm resulted in the blood flow projection images in the skin (Fig. 5(B)) and the brain cortex (Fig. 5(C)). For visual comparison, Fig. 5(D) gives the MAP projection image of the blood perfusion without the application of segmentation algorithm as described above.

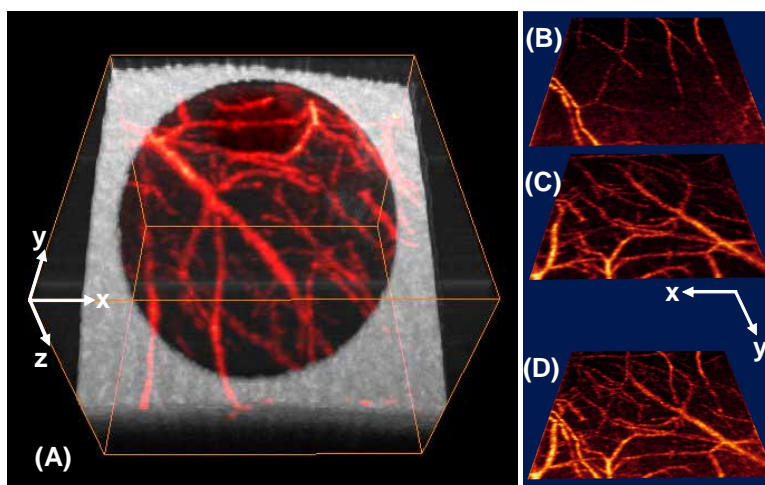


Fig. 5. Cerebral blood perfusion was imaged with OMAG *in vivo* with the intact skin and cranium. (A) volumetric rendering of fused 3D OMAG micro-structural and blood perfusion image. The volume size is $2.5 \times 2.5 \times 2.0 \text{ mm}^3$, see also the associated movie for details (2.6Mbytes); (B) projection image of blood flows from within the skin; (C) projection image of cerebro-vascular perfusion from brain cortex; and (D) Projection image from all depths.

In the next imaging experiment, we used OMAG to obtain multiple 3-D images of the same mice brain with the skin and skull intact over different regions of the head. The scan was performed clockwise that resulted in six OMAG images covering an area of approximately $4.2 \times 7.2 \text{ mm}^2$ over the mouse head. The total imaging acquisition time required to scan such an area and to stream the spectral data from the camera into the host computer was 7.5 minutes. The volume segmentation algorithm as described above was then applied to the six OMAG images separately to isolate the blood perfusion signals within the skin from those coming from the mouse brain. The MAP images from different regions of head were finally combined as a mosaic. Fig. 6(A) shows the mapping of blood flows within the skin of the mouse, while the cerebro-vascular blood perfusion is given in Fig. 6(B). For comparison, the photograph of the head right after the OMAG imaging and the photograph of the brain cortex after removal of the skin and skull bone are shown in Fig. 6(C) and Fig. 6(D), respectively. From Fig. 6(C), seeing the blood vessels through the skin is almost impossible. However, OMAG offers the opportunity to visualize the cerebral blood perfusion through the skin and skull. Comparing between Fig. 6(B) and Fig. 6(D), excellent agreement on the major vascular network over the brain cortex is achieved. Furthermore, the smaller blood vessels not observed in the photograph of Fig. 6(D) can be seen in the OMAG images, indicating the OMAG capability to delineate the capillary level vessels. The capacity of OMAG to achieve such high resolution imaging of the cerebral cortex – within minutes and without the need for dye injections, contrast agents, removal of skin or surgical craniotomy, - makes it an extremely valuable tool for studying the hemodynamics of the brain. This may give great potential for OMAG in the investigations of neurological diseases and brain functions in small animal models, for example, ischemic thrombotic stroke and neurological responses to sensory stimulations, which are widely studied in small animal models such as the genetically altered mouse.

It should be noted that the OMAG imaging of blood flow is only sensitive to the z component, i.e. flow velocity projected onto the probe beam direction. This is because the imaging is relied on the Doppler frequency induced in the optical interferogram by the moving blood cells. If a blood cell moves at a velocity of v , then the Doppler frequency

induced in OMAG signal will be $f_D = 2v \cos(\theta) / \lambda$, where θ is the angle between the probe beam direction and the blood flow direction, and λ is the center wavelength of the light source used. It is obvious that if $\theta = 90^\circ$, $f_D = 0$. As a consequence, OMAG is not sensitive to the transverse blood flow. This could however be amended if one carefully positions the OMAG probe beam so that $\theta \neq 90^\circ$ for the targeted tissue volume. Another solution maybe to use a dual-system with the probe-beam from each system pointing to the tissue sample at a different angle, or imaging is being performed by two consecutive scans to the same tissue volume while one changes the angle of OMAG probe beam in the second scan relative to the first scan. In this case, imaging time and computational effort will inevitably be increased.

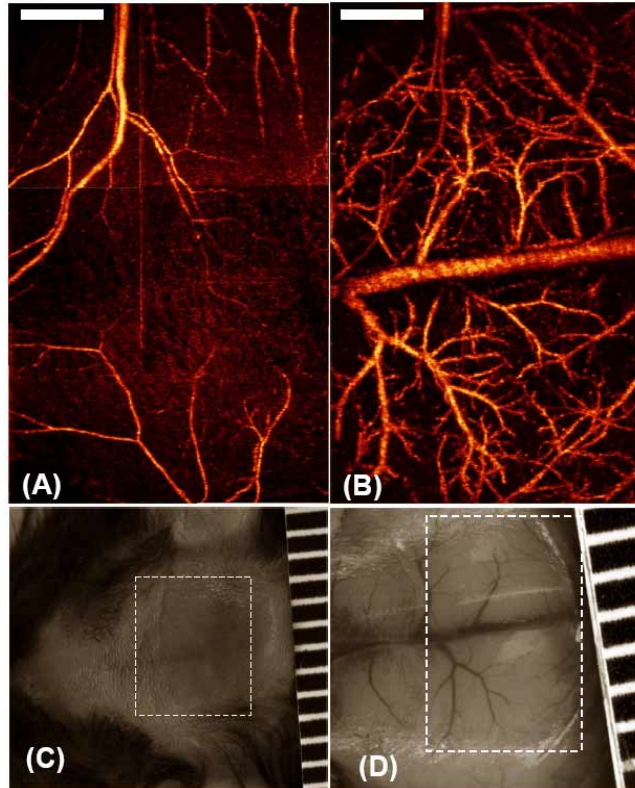


Fig. 6. The head of an adult mouse with the skin and skull intact was imaged with OMAG *in vivo*. (A) and (B) are the projection views of blood perfusion from within the skin and the brain cortex, respectively. Capillary blood flow can be seen from (B). It took ~7.5 minutes to acquire the 3-D data to obtain (A) and (B) using the current system setup. (C) Photograph taken right after the experiments where viewing the vasculatures through the skin is impossible. (D) Photograph showing blood vessels over the cortex after the skull and the skin of the same mouse were carefully removed. The superficial major blood vessels show excellent correspondence with those in (B). The area marked with dashed white box represents 4.2 by 7.2 mm²; and the scale bar indicates 1.0 mm.

The acquisition time for a full 3D data volume was ~50 seconds in the current study. This acquisition time was partially limited by the output power of the light source employed in the system. The imaging acquisition time can be shortened by a number of ways in order to investigate the functional changes in the brain that occur on a time scale shorter than ~50 seconds. With the spatial resolution fixed, one obvious approach is to increase the OMAG imaging speed by employing a higher power light source and a faster infrared InGaAs CCD

camera. However, if one does not need a high spatial resolution, the OMAG imaging can be configured to acquire less B scans that consist of C scan so that the imaging time is shortened.

4. Conclusions

Because of the increased penetration depth at 1.3 μm in biological tissue compared to that of ~800nm band light source, an optical micro-angiography imaging system has been constructed and demonstrated for *in vivo* imaging by employing a broadband SLD with central wavelength at 1.3 μm . The system was based on the spectral domain configuration with a high speed InGaAs line scan camera for spectrogram detection, similar to the spectral domain optical coherence tomography. We have shown that the system is capable of volumetric imaging of micro-structural morphology and blood perfusion in parallel of tissue samples *in vivo*. With this OMAG imaging system, we have obtained high quality and spatially resolved cerebrovascular blood perfusion images of live mice down to capillary level resolution through the intact skin and cranium without the interference of the blood perfusion from within skin. More important, no exogenous contrasting agents are necessary because the imaging contrast of OMAG is based on the endogenous light scattering signals. Without the need for dye injections, contrast agents, removal of skin or surgical craniotomy, the results demonstrate the potential of 1.3 μm OMAG as a high resolution and high sensitivity imaging tool in the investigations of cerebrovascular diseases in small animal models.

Acknowledgment

This research was made possible with generous support from Department of Biomedical Engineering, Oregon Health & Science University.